3420–3431 *Nucleic Acids Research, 2016, Vol. 44, No. 7* *Published online 10 February 2016*
doi: 10.1093/nar/gkw082

The crystal structure of human GlnRS provides basis for the development of neurological disorders

Jana Ognjenović[1], Jiang Wu[2], Doreen Matthies[3], Ulrich Baxa[3], Sriram Subramaniam[3], Jiqiang Ling[2,*] and Miljan Simonović[1,*]

[1]Department of Biochemistry and Molecular Genetics, University of Illinois at Chicago, Chicago, IL 60607, USA, [2]Department of Microbiology and Molecular Genetics, The University of Texas, Health Science Center at Houston, Houston, TX 77030, USA and [3]Laboratory of Cell Biology, Center for Cancer Research, National Cancer Institute, National Institutes of Health, Bethesda, MD 20892, USA

Received November 30, 2015; Revised January 29, 2016; Accepted February 01, 2016

ABSTRACT

Cytosolic glutaminyl-tRNA synthetase (GlnRS) is the singular enzyme responsible for translation of glutamine codons. Compound heterozygous mutations in GlnRS cause severe brain disorders by a poorly understood mechanism. Herein, we present crystal structures of the wild type and two pathological mutants of human GlnRS, which reveal, for the first time, the domain organization of the intact enzyme and the structure of the functionally important N-terminal domain (NTD). Pathological mutations mapping in the NTD alter the domain structure, and decrease catalytic activity and stability of GlnRS, whereas missense mutations in the catalytic domain induce misfolding of the enzyme. Our results suggest that the reduced catalytic efficiency and a propensity of GlnRS mutants to misfold trigger the disease development. This report broadens the spectrum of brain pathologies elicited by protein misfolding and provides a paradigm for understanding the role of mutations in aminoacyl-tRNA synthetases in neurological diseases.

INTRODUCTION

Aminoacyl-tRNA synthetases (aaRSs), ubiquitously expressed enzymes in organisms from bacteria to humans, play a vital role in ensuring accurate translation of the genetic information into functional proteins (1). These enzymes couple each of the 20 standard proteinogenic amino acids to a defined set of isoacceptor tRNAs capable of 'reading' specific codons in the mRNA. Thus, aaRSs decode a three-letter cipher written in the anticodon loop of tRNA into a single letter code of the protein language. The error rate of the tRNA aminoacylation reaction correlates well with the overall error rate of protein synthesis, and it is largely accepted that the accuracy of aaRSs dictates fidelity of gene translation (2,3). In addition to the canonical role in translation, aaRS have also evolved new functions through acquisition of novel domains and alternative splicing (4–6).

Recent advances in genome sequencing and human genetics have revealed a large number of disease-causing mutations in human aaRSs (7,8). The first study suggesting a causative link between mutations in an aaRS gene and human diseases was reported more than a decade ago (9). Multiple mutations in *GARS* (encoding cytosolic glycyl-tRNA synthetase) cause the Charcot–Marie–Tooth Type 2D (CMT2D) and distal spinal muscular atrophy type V, both inherited peripheral neuropathies characterized by impaired motor function, sensory loss in extremities, and spinal cord atrophy (9). Subsequent studies revealed that mutations in cytosolic *YARS*, *AARS* and *KARS* are also associated with CMT (10–12), while those in *HARS* cause deaf-blindness (13). The importance of aaRSs for the development of a healthy human organism is not restricted to the cytosolic enzymes. Initially, the evidence suggested a pattern in which mutations in cytosolic aaRSs largely affected the peripheral nervous system and those in the mitochondrial variants impacted a more diverse set of physiological processes (14–22). However, recent studies have shown that cytosolic aaRSs are vital for the development of the central nervous system as well. In particular, mutations in *DARS* cause hereditary leukoencephalopathy characterized by hypomyelination of the brainstem, spinal cord involvement, and leg spasticity (23,24). Also, mutations in *MARS* are linked to hereditary spastic paraplegias (24) and those in *KARS* cause severe infantile visual loss, progressive microcephaly, developmental delay, seizures, and abnormal subcortical white matter (25). Interestingly, not all mutations affect canonical functions of the given aaRS (i.e. catalysis, tRNA binding), but they may alter the enzyme's structure and/or its non-canonical function(s) (reviewed in (26,27)).

*To whom correspondence should be addressed. Tel: +1 312 996 0059; Fax: +1 312 413 0353; Email: msimon5@uic.edu
Correspondence may also be addressed to Jiqiang Ling. Tel: +1 713 500 5577; Fax: +1 713 500 4499; Email: Jiqiang.ling@uth.tmc.edu

Most recently, four distinct compound heterozygous mutations of the highly conserved residues in human *QARS* gene (encoding glutaminyl-tRNA synthetase, or GlnRS) have been shown to cause severe disorders of the central nervous system in two nonconsanguineous families (28). In one family, a patient carried G45V and R403W mutations on separate copies of the *QARS* gene, and in the other, Y57H and R515W substitutions were imprinted in separate alleles. Remarkably, the unrelated patients displayed a common phenotype characterized by progressive microcephaly, severe and intractable infant epilepsy, and diffuse atrophy of the cerebral cortex and cerebellum (MCPH). The study has shown that mutations located near the N-terminus decreased the GlnRS activity and that those closer to the C-terminus caused a complete loss-of-function. However, it remained unclear how exactly these genetic alterations affect the structure and function of GlnRS, and perhaps more importantly, how they could cause a dramatic deterioration of the human brain.

Human GlnRS (hGlnRS), a member of class I aaRS enzymes, is responsible for synthesis of the cytosolic pool of glutaminyl-tRNA^{Gln} (Gln-tRNA^{Gln}) and is, therefore, essential for incorporation of L-glutamine (Gln) into all proteins translated in the cytosol. In a canonical reaction cycle, GlnRS activates Gln with ATP and forms glutaminyl adenylate. The amino acid is subsequently transferred onto the 2′ hydroxyl of A76 in tRNA^{Gln}. Early structural studies have shown that the bacterial enzyme comprises the catalytic and anticodon-binding domains that recognize Gln and tRNA^{Gln}, respectively (29). However, in contrast to the bacterial enzyme, human and eukaryotic GlnRSs contain an appended ≈200 amino acids long N-terminal domain (NTD). This distinct, and among eukaryotes ubiquitous, extension is important for formation of the multisynthetase complex (MSC) (30,31) and for propagating anti-apoptotic signals through interactions with apoptosis signal-regulating kinase 1 (ASK1) (32). Attempts to study idiosyncrasies of the eukaryotic system using the fungal GlnRS yielded two incomplete structures: one composed solely of the NTD (33), and the other comprised of the catalytic and anticodon-binding domains (34). These studies, whereas important to reveal the local structures of the domains in a eukaryotic GlnRS, could not ascertain if the spatial arrangement and interactions between the domains play any role in regulating activity of the human enzyme. Moreover, the low level of sequence conservation between the yeast and mammalian orthologs hindered construction of a reliable model of the human GlnRS that could facilitate our understanding of the effect(s) of pathological mutations.

Herein, we provide a detailed structural, biophysical and enzymatic characterization of the intact human cytosolic GlnRS. Our results reveal the structure of a complete eukaryotic GlnRS, the structure of its NTD in the context of the intact enzyme and the three-dimensional arrangement of all domains. The findings presented herein suggest that a combination of an allele encoding a catalytically inefficient enzyme and an allele encoding a misfolded mutant enzyme is a likely cause for the severe deficiency in GlnRS activity in the patients.

MATERIALS AND METHODS

Protein expression and purification

The gene encoding human GlnRS was cloned into pET28a with an N-terminal His-tag. GlnRS was overexpressed in Rosetta(DE3)pLysS cells at +16°C in the presence of 0.5 mM IPTG for 16 h, and then purified using the HisTrap FF Crude Ni^{2+}-affinity and the Superdex 200 size-exclusion columns (GE Healthcare Life Sciences). Fractions containing higher order oligomers and monomeric GlnRS were pooled separately and concentrated in 25 mM Tris, pH 8.0, 300 mM NaCl and 5% (v/v) glycerol. Protein crystallization and data collection is described in SI.

Crystallization and data collection

Crystals of hGlnRS were obtained in a sitting drop setup at +16°C. The apo wild type (WT) hGlnRS crystallized in 0.1 M calcium acetate, 0.1 M Tris, pH 6.0, 12.5% (w/v) PEG 3,350, 60 mM Gly-Gly-Gly. The Y57H mutant crystallized in 0.1 M ammonium acetate, 0.1 M Bis-Tris, pH 5.5 and 17% (w/v) PEG 10 000, whereas the crystals of the G45V variant were obtained from 0.15 M ammonium acetate, 0.1 M Bis-Tris, pH 5.5, 3% (w/v) PEG 20 000 and 10 mM EDTA. Prior to data collection, crystals were cryoprotected in the mother liquor supplemented with 28% (v/v) glycerol and flash frozen in liquid nitrogen. The diffraction data were collected at the liquid nitrogen temperature. The SAD data set used for selenium phasing of the hGlnRS crystals was collected at the LS-CAT beam station ($\lambda = 0.9795$ Å). The data sets used for structure refinement were collected under the same conditions at either the LS-CAT (for WT hGlnRS and Y57H) or GM/CA@APS (for G45V) beam stations (Table 1).

Structure determination and refinement

The diffraction images were processed in HKL2000 (35). Selenium sites were located using SHELX (36), the experimental phase was calculated in MLPHARE (37) ($R_{cullis,ano} = 0.72$; figure of merit = 0.32 at 3.7 Å; anomalous $f'' = 1.14$), and the phase estimates were improved by solvent flattening and histogram matching in DM (38,39). Iterative structure refinement and model building was completed using Phenix (40) and Coot (41). The superimpositioning analysis was done using Cealign (42) and all figures were generated in PyMOL (43).

In vitro aminoacylation assays

GlnRS activity was determined as previously described (28) using 10–500 nM GlnRS, 0.2–8 μM human cytoplamic tRNA^{Gln} transcripts, 2 mM ATP and 50 mM [^{3}H] L-Gln (320 cpm/pmol) in 100 mM HEPES-NaOH, pH 7.2, 30 mM KCl and 10 mM $MgCl_2$ at +37°C. Aliquots were spotted on 3MM Whatman paper discs presoaked with 5% trichloroacidic acid (TCA), washed three times with 5% TCA, dried, and their radioactivity level was measured in the scintillation counter.

Table 1. Data collection and refinement statistics

	WT hGlnRS	G45V	Y57H
Data collection			
Space group	$P\,2_12_12$	$P\,2_12_12$	$P\,2_12_12$
Cell dimensions			
a, *b*, *c* (Å)	333.7, 57.9, 86.1 $\alpha = \beta = \gamma = 90^\circ$	336.9, 58.5, 86.6 $\alpha = \beta = \gamma = 90^\circ$	333.1, 58.3, 85.1 $\alpha = \beta = \gamma = 90^\circ$
Wavelength (Å)	0.9792	1.0332	0.9792
Resolution (Å)	50.00–2.40	50.00–2.70	50.00–3.30
R_{pim}*	0.056 (0.866)	0.099 (0.853)	0.118 (0.714)
CC1/2	0.81	0.55	0.82
I/σ (I)*	8.75 (0.88)	4.94 (0.90)	8.35 (1.37)
Completeness (%)*	98.2 (83.4)	99.1 (99.6)	99.9 (99.7)
Redundancy*	4.9 (5.0)	3.8 (3.8)	4.8 (4.9)
Refinement			
Resolution (Å)	29.00–2.40	49.00–2.70	34.00–3.30
No. reflections	66,515	47,742	25,874
R_{work}*	0.211 (0.332)	0.228 (0.361)	0.221 (0.305)
R_{free}*	0.239 (0.353)	0.262 (0.382)	0.274 (0.372)
Number of atoms	5,477	5,288	5,171
Protein	5,240	5,201	5,153
Water	237	87	18
Ramachandran statistics			
Favored (%)	92.0	87.0	84.0
Outliers (%)	0.7	0.7	0.7
B-factors	76.7	94.9	68.0
Protein	77.6	95.4	68.1
Water	58.7	65.1	46.8
R.m.s. deviations			
Bond lengths (Å)	0.011	0.010	0.014
Bond angles (°)	1.35	1.60	1.91

* - Statistics for the highest-resolution shell are shown in parentheses.

Electrophoretic and mass spectrometry analysis of GlnRS mutants

Purified WT and mutant GlnRS samples (2.5 μg) were analyzed on Mini-Protean TGX Stain-Free SDS-PA gels. Specific bands were excised from the gel and further analyzed by mass spectrometry at the core facility, the Research Resource Center, University of Illinois at Chicago (Chicago, IL). The western blot analyses were performed on samples under reducing conditions. Following separation on either SDS-PA or native 4–16% Bis-Tris Native PA (Life Technologies) gels, the protein bands were transferred onto a PVDF membrane. The GlnRS bands were detected using anti-GlnRS mouse antibody (Santa Cruz Biotechnology) and anti-mouse IgG coupled with horseradish peroxidase (Qiagen), while the GroEL bands were detected using rabbit anti-GroEL antibody and anti-rabbit IgG horseradish peroxidase conjugate (Sigma Aldrich). An enhanced chemiluminescence (ECL) substrate kit (Amersham) was used for detection following standard manufacturer's protocols.

Thermal shift assay

Purified GlnRS (20μM) samples were mixed with the SYPRO-Orange dye (1:500 dilution; Sigma Aldrich) in a 4:1 ratio. Mixtures were dispensed into a 384-well microplate in triplicates and analyzed on the Vii^{TM} 7 Real-Time PCR System (Life Technologies) using the Melting Curve method with a continuous heating (0.075°C/s) from 25°C to 95°C. The melting curves were recorded in real time as change in fluorescence signal and analyzed using the ViiA^{TM} 7 RUO Software (Life Technologies).

Electron microscopy

Samples were diluted to ≈0.4 mg/ml, adsorbed to a freshly glow-discharged carbon-film grid for 15 s, and stained with 0.7% uranyl formate. Images were collected on an FEI Tecnai T12 with a 4k x 4k Gatan Ultrascan CCD camera at a pixel size of ≈0.46 and ≈0.18 nm/px.

RESULTS

The overall structure and domain arrangement in intact human GlnRS

To enable precise biochemical and functional studies on hGlnRS and its mutants, we determined by selenomethionine SAD phasing the crystal structure of the complete apo hGlnRS to 2.36-Å resolution (Table 1, Figure 1 and Supplementary Figure S1). Intact hGlnRS crystallized in the primitive orthorhombic crystal lattice with one molecule in the asymmetric unit (Table 1).

Human GlnRS is a monomeric class I aaRS composed of 775 amino acids. The enzyme adopts a boomerang-like shaped structure built of 5 domains that span ≈100 × 90 × 40 Å (Figure 1A). One boomerang wing is composed of an appended NTD (residues 1–182) that is linked to the second wing by a long and flexible hinge domain. An 8-helical bundle (N1) and a 3-helical tail (N2) form a bi-lobed

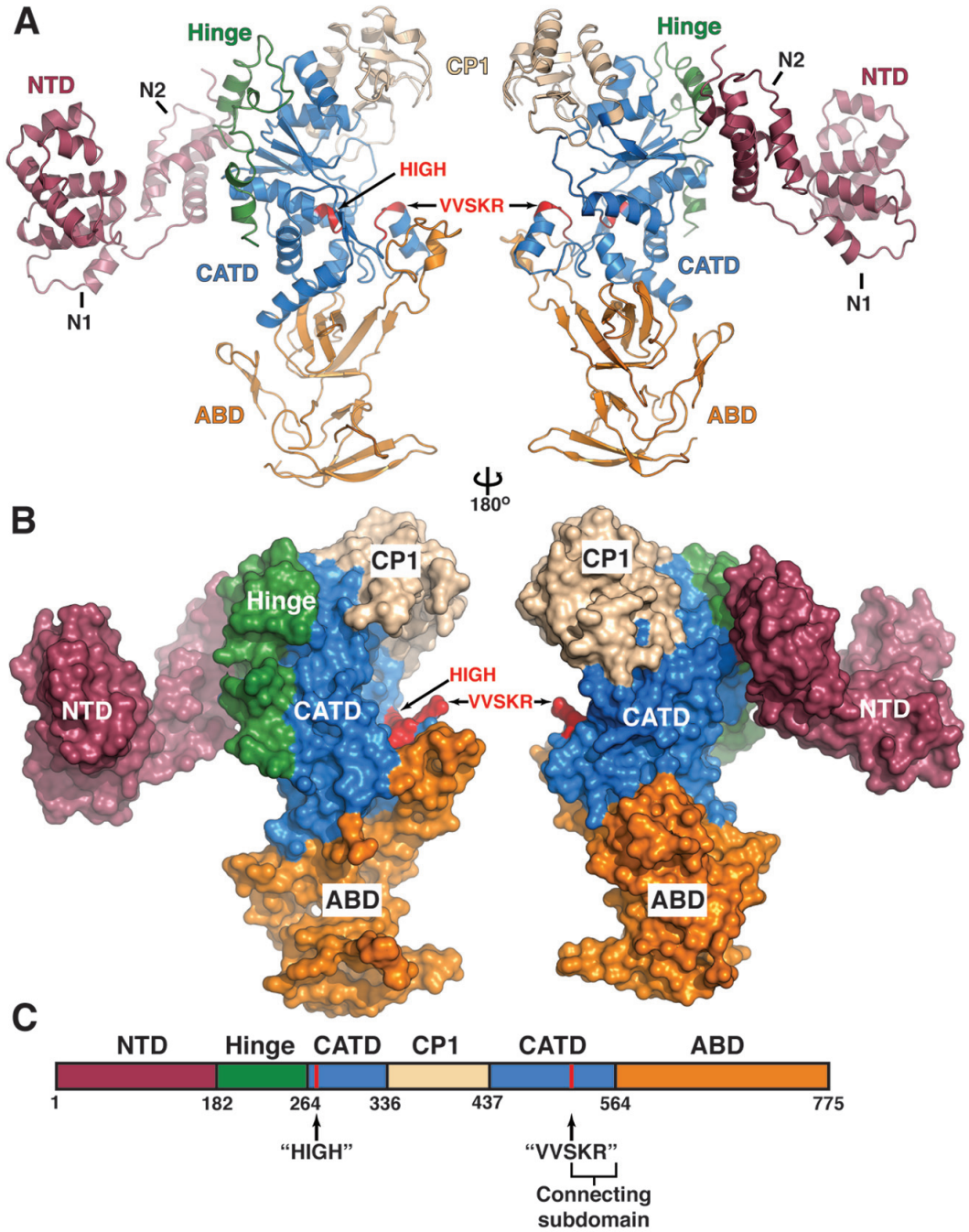

Figure 1. Overall structure and domain organization of the intact human GlnRS. **(A)** A cartoon representation of two views of the intact structure of human GlnRS. Domains are labeled as in the main text and colored according to scheme in (C). (**B**) A surface representation diagram of the structure of hGlnRS in the same orientation as in (A). (**C**) Domain structure with domain names and coloring scheme. The conserved motifs, 'HIGH' and 'VVSKR', and connecting subdomain are indicated. Agreement between the final model and electron density maps is shown in Supplementary Figure S1.

structure of NTD that protrudes from the enzyme body. An 82-residue long hinge connects the N2 subdomain to the catalytic domain (CATD; residues 264–335 and 438–564). While the first part of the hinge, covering residues 183–216, is disordered, the second part adopts a predominantly α-helical structure that intimately interacts with CATD (Figure 1A). Following the ordered part of the hinge, the first β-strand of the Rossmann fold and a conserved 'HIGH' motif (^{277}HIGH^{280}) emerge. In a canonical fashion, the Rossmann fold is split after its third β-strand with an insertion designated as connecting peptide 1 (CP1; residues 336–437). CP1 adopts a mixed α/β structure that sits atop CATD where it forms the roof of the active site (Figure 1). The second half of the Rossmann fold continues from the fourth β-strand and it eventually grows into a connecting subdomain (residues 498–564), which links CATD with the anticodon-

binding domain (ABD; residues 565–775). The connecting subdomain contains a poorly conserved 'KMSKS' motif whose exact sequence in hGlnRS is ^{493}VVSKR^{497} (Figure 1). The VVSKR is juxtaposed to the long penultimate β-strand of CATD and it precedes the helical segment and a short, partially disordered terminal β-strand (residues 541–548) that complete the Rossmann fold. The C-terminal ≈230 amino acids of hGlnRS form ABD, which is folded into an all β structure that belongs to the superfamily of ribosomal protein L25-like proteins (Figure 1A). Unlike the rest of the structure, several segments in ABD (e.g. residues 585–588, 630–638 and 668–673) are disordered in our crystal. This is not surprising because the majority of crystal lattice contacts in our crystal are established between the symmetry related NTDs and CATDs.

Distinct structural features of the intact human GlnRS

Although it was presumed that structures of human, bacterial and yeast GlnRSs would be similar, attempts to phase crystals of the intact human enzyme by molecular replacement using yeast and bacterial GlnRS structures as search models failed. A comparative structural analysis reveals that the structure of human GlnRS is distinct when compared to structures of other orthologs.

First, we compared the structure of NTD from hGlnRS with the corresponding domain in *Saccharomyces cerevisiae* GlnRS (*Sc*GlnRS) as well as with the C-terminal region of B subunit of the *Staphylococcus aureus* GatCAB amidotransferase (GatB) (44). It has been shown that NTD of *Sc*GlnRS binds tRNA^{Gln} and that it is structurally similar to GatB (33). It is therefore plausible that the NTD from hGlnRS and GatB are structural homologs as well. The superimposition of the entire NTD yields surprisingly large r.m.s.d. values of 4.1 Å for *Sc*GlnRS and 5.8 Å for GatB (Figure 2A,B). A closer inspection reveals that the main source of structural divergence stems from different arrangements of helical segments within the N1 subdomain (Supplementary Figure S2A). Although containing only 6 α-helices, the N1 subdomain of *Sc*GlnRS superimposes reasonably well onto the human N1 (r.ms.d. of 2.65 Å; see Supplementary Figure S2A). By contrast, the N1 subdomain of the human enzyme contains an additional α-helix at its N-terminus, while the corresponding segment in GatB has an inserted helical element between α4 and α6 (Supplementary Figure S2B). This explains a large r.m.s.d. value of 4.8 Å obtained after superimpositioning of these two subdomains. On the other hand, the superimposition of the N2 subdomain from hGlnRS onto that of *Sc*GlnRS and GatB yields r.m.s.d. values of 1.64 Å and 2.8 Å, respectively, suggesting that the structure of the N2 subdomain is relatively conserved from bacteria to mammals. (Supplementary Figure S2C,D).

The structural differences in NTD prompted us to speculate that this domain may be important for enzymatic function of human GlnRS. To test our hypothesis, we created two truncation mutants that lacked either the N1 subdomain (ΔN1) or the entire NTD (ΔNTD). Our results show that both truncations significantly reduce the aminoacylation activity of hGlnRS (Table 2). This raised an interesting question whether the orientation of NTD relative to the CATD is important for GlnRS function. A closer inspection revealed that the imidazole ring of His175 in NTD forms a hydrogen bond with the side chain of Gln263 in the hinge domain that interacts closely with the CATD domain (Supplementary Figure S2E). To assess if this interaction is functionally important, we mutated His175 to Ala (H175A) and determined the catalytic activity of the mutant enzyme. Our kinetic data show that the catalytic efficiency of H175A is decreased approximately 60-fold when compared to the wild-type (WT) enzyme (Table 2), which suggests that proper positioning of the NTD is important for the activity of GlnRS.

Next, we compared structures of other domains in hGlnRS. Because of the partial disorder in our crystal form, we excluded the hinge domain from our analysis. The superimposition of CATD, CP1 and ABD from hGlnRS onto the corresponding domains in *Sc*GlnR and *Escherichia coli* GlnRS (*Ec*GlnRS) yields relatively high r.m.s.d. values of 3.5 Å and 3.3 Å, respectively (Figure 2C,D). Despite the conservation of the overall domain arrangement, a number of structural elements in human enzyme differ from the bacterial and fungal homologs. In hGlnRS, a short and disordered loop connects strand β4 with helix α19 in CP1. On the contrary, this loop is enlarged and ordered in the bacterial and yeast enzymes (Supplementary Figure S3A,B). Further, a short α-helix between strands β5 and β6 in CP1, which is conserved in bacteria and yeast, is absent from hGlnRS (Supplementary Figure S3A,B). Also, in ABD, a long linker composed of three loops and three α-helices connecting strands β22 and β23 in *Sc*GlnRS is replaced by a much shorter loop in the human enzyme (Supplementary Figure S3C). These observations led us to hypothesize that structural differences may be reflected at the functional level.

Because GlnRS was horizontally transferred from eukaryotes to bacteria (45), we decided to test if the human enzyme is capable of charging bacterial tRNA^{Gln} and *vice versa*. To our surprise, our results show that hGlnRS cannot aminoacylate bacterial tRNA^{Gln} and that *Ec*GlnRS cannot act on human tRNA^{Gln} (Figure 2E). Taken together, our results argue that the structure of hGlnRS is distinct from other orthologs, particularly bacterial GlnRS, and that structural and functional conservation of the GlnRS system is lost from bacteria to eukaryotes including mammals. A recent study shows that human GlnRS is able to complement a yeast strain lacking GlnRS (46), indicating that recognition of tRNA^{Gln} by human and yeast GlnRSs may be conserved.

Mutations G45V and Y57H modestly affect the conformation of NTD and stability of GlnRS

The structure of hGlnRS enabled precise mapping of mutations implicated in the development of neurological disorders. We have previously shown that the G45V and Y57H mutations, which are located in the NTD, decrease the aminoacylation activity of hGlnRS (28). To understand how these pathological mutations affect the enzymatic reaction, we determined the kinetic parameters for both the WT and mutant hGlnRS constructs (Table 2). The G45V and Y57H mutations decreased the k_{cat}/K_m ratio by 10- and 220-fold, respectively. It has previously been proposed that

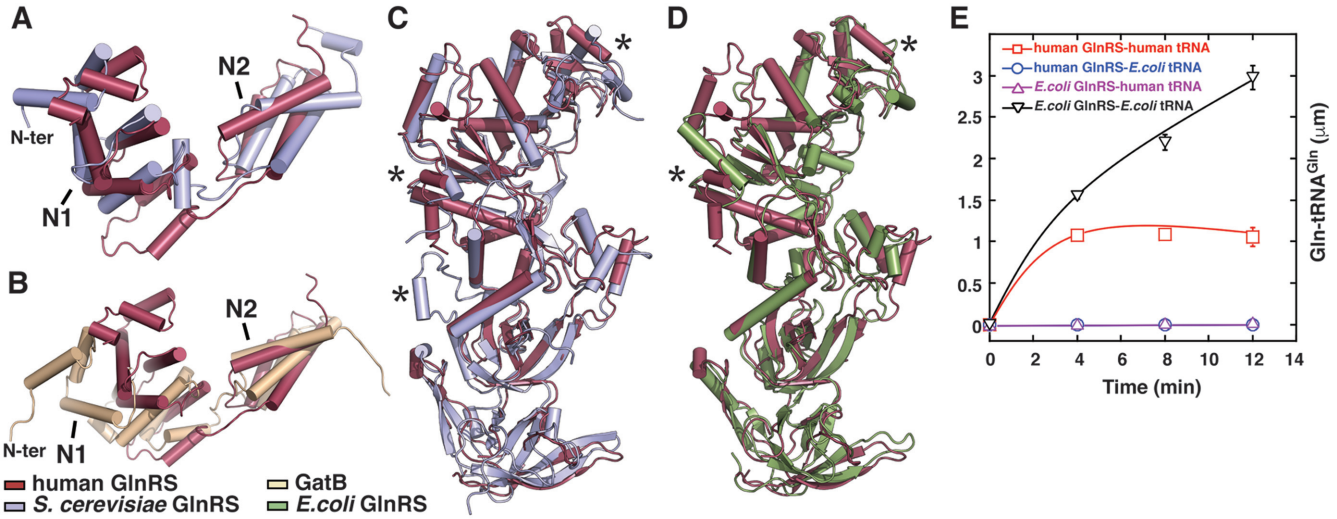

Figure 2. Structural comparison of domains in human, yeast and bacterial GlnRSs. (**A**,**B**) The global superimpositioning of NTDs from human and yeast GlnRS, and GatB reveals significant structural divergence in spite of the overall conservation of the domain architecture (see Supplementary Figure S2). (**C**,**D**) The superimpositioning of core domains (CATD, CP1 and ABD) in yeast and bacterial GlnRSs onto that in human GlnRS shows that although the overall fold is conserved, there are significant structural differences in the CP1 and anticodon-binding domains (marked by asterisks; see Supplementary Figure S3). (**E**) Enzymatic results show the loss of orthogonality between human and *E. coli* GlnRS and tRNAGln pairs.

Table 2. Aminoacylation kinetics of GlnRS variants for $tRNA^{Gln}$

GlnRS variants	k_{cat} (min^{-1})	K_m (μM)	k_{cat}/K_m (μM^{-1} min^{-1})	Fold change (k_{cat}/K_m)
WT	12.2 ± 5.0	0.67 ± 0.15	17.8 ± 4.5	1.0
ΔN1 (116–775)	0.09 ± 0.01	1.5 ± 0.4	0.07 ± 0.01	270
ΔNTD (183–775)	ND[a]	ND	ND	ND
G45V	0.89 ± 0.43	0.53 ± 0.06	1.7 ± 0.8	10
Y57H	0.12 ± 0.04	1.7 ± 0.8	0.08 ± 0.04	220
H175A	0.20 ± 0.03	0.60 ± 0.23	0.39 ± 0.23	46
R403W	ND	ND	ND	ND
R515W	ND	ND	ND	ND

[a]ND, no detectable activity.

the NTD of *Sc*GlnRS may be important for tRNA binding (33). However, our results show that, instead of affecting the K_m for $tRNA^{Gln}$, both G45V and Y57H caused a significant decrease in k_{cat}, which, in turn, suggests that these mutations cause a long-range effect on the distal CATD. In agreement with this, the H175A mutation, which disrupts the interaction between the NTD and CATD, also affected only the k_{cat} and not the K_m (Table 2).

To further explain the mechanism at the structural level by which these genetic alterations may affect the catalysis of GlnRS, we determined the crystal structures of the G45V and Y57H mutants (Table 1). The N1 subdomain harbors Gly45 and Tyr57, residues mutated in patients affected with the neurological disorder. Gly45 is in the solvent-flexible loop between helices α4 and α5 (Supplementary Figure S4A), and Tyr57 is in the middle of helix α5 (Figure 3A). The aromatic ring of Tyr57 stacks against the aliphatic side chain of Leu15, which resides in a loop between helices α1 and α2 (Supplementary Figure S4B). Overall structures of the two NTD mutants are similar to the structure of the WT hGlnRS, which is illustrated by low r.m.s.d. values of 0.65 Å and 0.97 Å calculated after superimposition of the WT hGlnRS onto G45V and Y57H, respectively (Figure 3B,C). However, structural rearrangements of different magnitude occur in the NTD of both mutants. The G45V mutation causes a relatively minor conformational change in the α4-α5 loop, which is rotated toward CATD in the mutant enzyme (Figure 3B). On the other hand, the entire NTD rotates ≈3° toward the CATD in the Y57H mutant structure (Figure 3C). Consequently, Y57H adopts a more closed conformation when compared to the WT hGlnRS.

Because both G45V and Y57H hGlnRS mutants express at a similar level and form stable monomers in solution as the WT enzyme, we were puzzled as to why these particular mutants would exhibit lower level of enzymatic activity. We postulated that, besides the NTD conformation, G45V and Y57H might have affected the enzyme stability as well. To ascertain if this is the case, we employed a thermal shift assay. The melting curve of the WT hGlnRS exhibits a single peak with the melting temperature (T_m) of +47.5°C (Figure 4A). The presence of a single peak suggests that the WT enzyme unfolds according to a simple two-state model. The melting curves of G45V and Y57H, however, comprise two peaks indicating that these mutants unfold along a more complex trajectory (Figure 4A). The

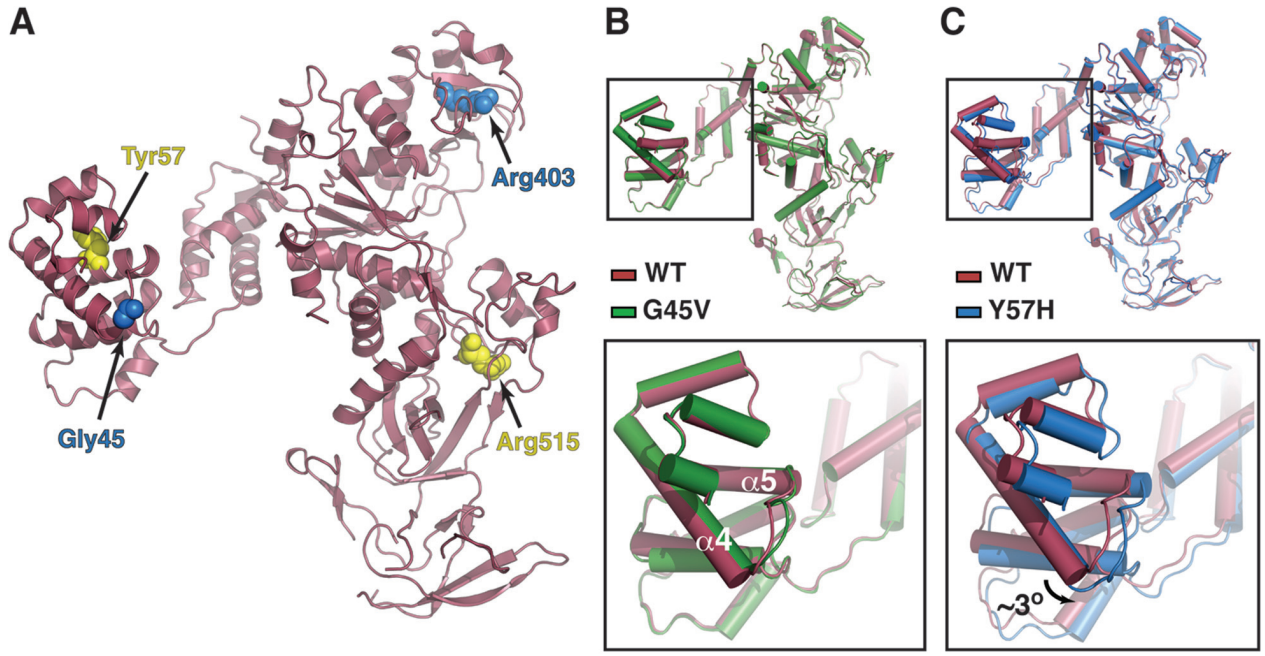

Figure 3. The pathological mutations, G45V and Y57H, mildly affect the structure and conformation of NTD in human GlnRS. (**A**) Four mutations implicated in the development of neurological disorder are mapped onto the structure of hGlnRS. Two mutations, G45V and Y57H, are located in NTD, R403W is in CP1 and R515W is in CATD. The pairs of mutations found in different patients are colored blue (G45V and R403W) and yellow (Y57H and R515W). (**B**) The crystal structure of G45V is similar to that of the WT hGlnRS. A minor structural rearrangement is present in the loop connecting helices α4 and α5 in NTD. (**C**) The superimposition of Y57H onto hGlnRS reveals that NTD rotates ≈3° toward the CATD in the mutant structure. A close-up view of structural differences in NTDs is shown in the box in (**B**), and (C).

(un)folding events occur at +46.5°C and +52°C in G45V, and at +46°C and +51°C in Y57H (Figure 4A).

Taken together, the overall structure of NTD mutants is similar to that of the WT hGlnRS, but the conformation and orientation of NTD in these mutants is slightly altered. Moreover, point mutations in NTD alter the stability and folding trajectory of the enzyme, which may explain why the catalytic activity of G45V and Y57H are decreased compared to the WT enzyme.

Pathogenic mutations mapping in CP1 and CATD cause misfolding and aggregation of GlnRS

Besides a *QARS* allele encoding a mutation that maps within the NTD, each patient also carried a second allele that encoded a mutation located closer to the C-terminus of GlnRS. The patients were reported to carry either R403W or R515W mutation (28). In contrast to relatively mild effects of NTD mutations, both Arg->Trp substitutions caused a more dramatic loss of GlnRS function (28). Because it remained unclear how replacing an Arg residue with Trp could impact the GlnRS function so dramatically, we embarked on structural characterization of R403W and R515W.

The crystal structure of hGlnRS provides a platform for examining the role Arg403 and Arg515 play in the native structure (Figure 3A, Supplementary Figure S4). The side chain of Arg403 is located in the second β-strand (β5) of the CP1 domain where it interacts with the side chain of Gln360 from the flexible β4-α15 loop and the backbone carbonyl oxygen of Asp414 in strand β6 (Supplementary Figure S4C). On the other hand, Arg515 is in the loop within the helical subdomain that links CATD and ABD (Supplementary Figure S4D). This particular loop is spatially positioned immediately below the VVSKR motif, with which it supports a long hairpin-like structure within ABD that is formed by strands β21 and β22 and connecting α-helices (Figure 3A). Our attempts to characterize structures of these two mutants were unsuccessful because of the major hurdles encountered during protein expression and purification. Although expressing at a similar level as the WT enzyme, R403W and R515W are significantly less soluble. This is especially true for R403W. Moreover, instead of forming a stable monomer in solution, soluble fractions of these two mutant enzymes appeared to form aggregates or complexes of higher molecular mass. The first evidence for this behavior was obtained after analyzing soluble Ni-affinity column eluates over the size-exclusion chromatography (SEC) column. R403W and R515W elute from the SEC column earlier than a monomeric WT hGlnRS or NTD mutants (Figure 4B). Also, unlike a protein that adopts a native structure, soluble fractions of R403W and R515W absorb UV light more intensely at 260 nm than at 280 nm, implying that Arg->Trp mutants form aggregates and/or other complexes in solution. Analysis on TBE-Urea and agarose gels ruled out the presence of RNA and/or DNA in these samples (data not shown). In addition, in contrast to defined T_m values obtained for the WT enzyme and NTD mutants (Figure 4A), the exact T_m could not be calculated either for R403W or R515W. Instead of having defined peaks, the melting curves of Arg->Trp mutants exhibit a continuous linear decrease of intensity over a wide

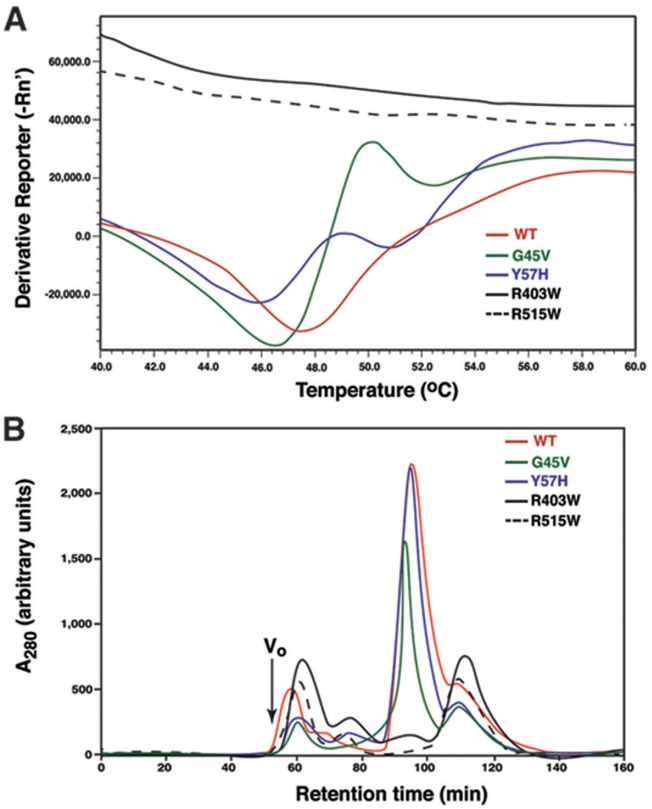

Figure 4. Effect of pathological mutations on the aggregation status and stability of GlnRS. (**A**) The melting curve of the WT hGlnRS (red line) exhibits a single peak with Tm of +47.5°C, whereas curves of G45V (green line) and Y57H (blue line) have two peaks with distinct minima at ≈+46°C and ≈+52°C. R403W (solid black line) and R515W (dashed line) exhibit a constant decrease in signal intensity without prominent peaks, suggesting formation of aggregates or other complexes. (**B**) Elution profiles of WT (red line), G45V (green line), Y57H (blue line), R403W (solid black line) and R515W GlnRS (dashed line) from the size-exclusion chromatography (SEC) column. WT, G45V and Y57H form predominantly monomers in solution (retention time ≈95 min), whereas R403W and R515W primarily form larger species that elute ≈60 min. Peaks eluting ≈110 min contain impurities.

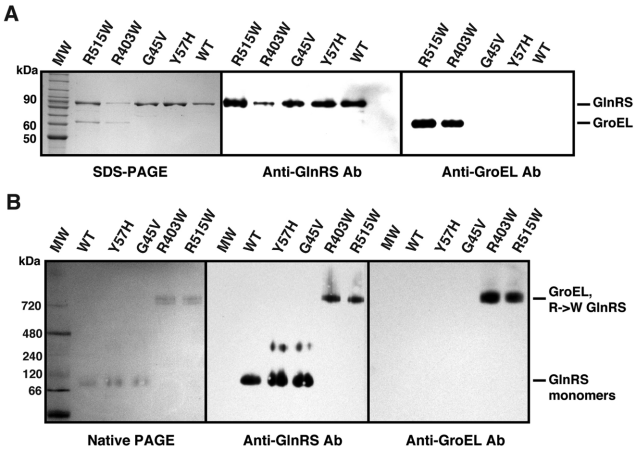

Figure 5. R403W and R515W mutants are bound to GroEL when recombinantly expressed in *E. coli* suggesting that they are misfolded. (**A**) SDS-PAGE (left panel) of purified GlnRS samples (R515W, R403W, G45V, Y57H and WT) reveals that only R->W mutants contain an additional protein band that runs at ≈60 kDa. The western blot with the anti-GlnRS antibodies (middle panel) demonstrates that all samples contain human GlnRS, whereas the same analysis with the anti-GroEL antibodies (right panel) shows that the 'aggregate' peaks of R->W mutants contain GroEL as well. (**B**) The native PAGE and subsequent western blots with anti-GlnRS (middle panel) and anti-GroEL (right panel) antibodies shows that WT, Y57H and G45V run as monomeric proteins (apparent molecular mass between 66 and 120 kDa), whereas R403W and R515W stably associate with GroEL and run as a single species of molecular mass above 720 kDa.

range of temperatures (Figure 4A), suggesting that these mutants either aggregate or do not adopt native structure in solution.

A routine SDS-PAGE analysis of the 'early' peaks showed that the Arg->Trp mutants contain an additional protein with molecular mass of ≈60 kDa (Figure 5A; left panel). The band pattern was persistent regardless of the expression protocol or sample treatment. We sought to determine the identity of the lower band by western blot analysis using anti-His antibodies. The antibodies recognized only the intact hGlnRS with an N-terminal His-tag (≈80 kDa), but not the lower band (data not shown). We speculated that the lower band could either be partially degraded mutant enzyme that is also prone to aggregation or another protein with which the Arg->Trp mutants perhaps formed a stable complex. Trypsin digestion and mass spectrometry revealed that the 60-kDa band is largely composed of GroEL and, to a far lesser extent, of the partially degraded GlnRS that is devoid of segments in both NTD (residues 1–34) and ABD (residues 652–775). Further, we probed samples with anti-GlnRS (Figure 5A, middle panel) and anti-GroEL antibodies (Figure 5A, right panel); the anti-GlnRS antibody reacted with the intact GlnRS in all samples and anti-GroEL antibody recognized only the 60-kDa band in the Arg->Trp mutant samples. It is important to note that the anti-GlnRS antibody targets the C-terminal portion of GlnRS and this perhaps explains the absence of its reactivity with the 60-kDa band. Hence, we cannot rule out that the lower band contains truncated hGlnRS as well. Analysis of the soluble fractions of R403W and R515W by negative-stain electron microscopy further reveals the ring structure of the GroEL complex (Figure 6). The collective results from the EM and biochemical analyses provide strong evidence that the 60-kDa band contains bacterial GroEL as a co-purifying component.

Next, we asked the question whether soluble fractions of R403W and R515W form oligomers that simply co-purify with GroEL or if the monomers of these mutants stably associate with the bacterial chaperonin. Based on the native PAGE analysis R403W and R515W have an apparent molecular mass of >720 kDa, which is almost an order of magnitude higher than that of the monomeric GlnRS (Figure 5B, left panel). Given that both anti-GlnRS and anti-GroEL antibodies react with the ≈720-kDa band (Figure 5B, middle and right panels), it was impossible to discern between the two scenarios based on this approach alone. We then attempted to separate GroEL from Arg->Trp mutants and to analyze those samples on the native PAGE. However, we observed that both mutant enzymes degrade quite rapidly when purified from GroEL (data not shown). Given

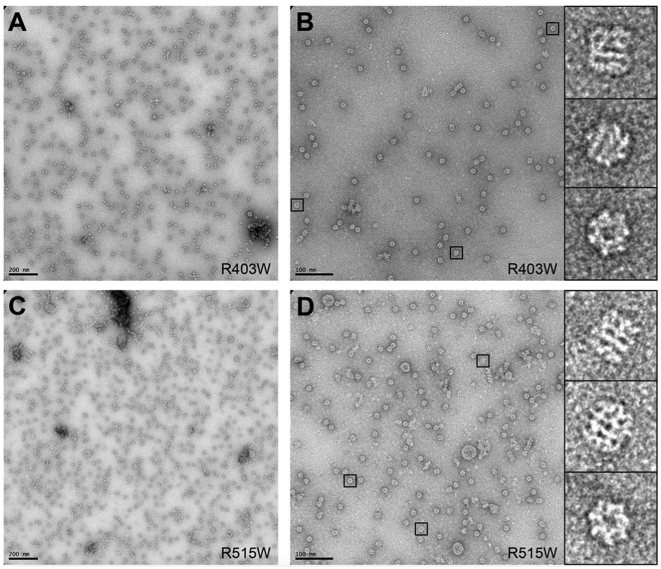

Figure 6. Negative-stain electron microscopy of hGlnRS R403W and R515W mutants. (**A**,**B**) Representative images of R403W mutant at different magnifications revealing a dominant population of GroEL particles. Three zoomed in insets are shown on the right displaying different views of the chaperonin. (**C**,**D**) Representative images of R515W mutant at different magnifications revealing a dominant population of GroEL particles. Three zoomed in insets are shown on the right displaying different views of the chaperonin. Size bars designate 200 nm in panels A and C, and 100 nm in panels B and D.

that EM images do not reveal the presence of higher order oligomeric structures other than GroEL, we conclude that soluble fractions of the Arg->Trp mutants of GlnRS most likely form a stable complex with GroEL.

In summary, R403W and R515W mutations cause misfolding of the enzyme and its tight association with the bacterial chaperonin. These mutants are also prone to degradation when separated from GroEL. The low solubility, misfolding and protease susceptibility are presumably the primary reasons for a dramatic loss-of-function in patients with Arg->Trp mutations of GlnRS.

DISCUSSION

Evolution and distinct structure of the human GlnRS

GlnRS is a late addition to the aaRS family that evolved from a non-discriminating glutamyl-tRNA synthetase after the split between archaea and eukaryotes (47,48). Although a vast majority of bacteria and archaea lack GlnRS and use an indirect pathway to produce Gln-tRNA^{Gln} (49,50), certain bacteria, such as *E. coli* and *Bacillus sp.*, have acquired GlnRS from eukaryotes through horizontal-gene transfer. In spite of the gene transfer (51), the bacterial GlnRSs do not contain the appended NTD, which is ubiquitously found in eukaryotic enzymes. However, it is not clear whether the NTD was lost during the gene transfer or if it represents a newly evolved feature in eukaryotic GlnRSs. The sequence conservation of the yeast and mammalian NTDs is rather poor and it levels off at 28%. This pales in comparison with ≈40% of the conserved residues in the corresponding CATD and ABD domains. The low level of sequence conservation is reflected at the structural level. Even the seemingly similar CATD and ABD domains of the human GlnRS differ from the counterparts in the yeast and bacterial enzymes. Also, a significant level of structural divergence is present in the N1 subdomain of NTD. However, it remains to be seen if these differences are important for the function of hGlnRS. Perhaps, studies on the hGlnRS-tRNA^{Gln} binary complex and larger assemblies of the MSC that require GlnRS could be informative about the functional significance of the noted structural differences.

Importance of the NTD for GlnRS function

The crystal structure presented here revealed the domain organization of the intact eukaryotic GlnRS for the first time. Importantly, the NTD domain was visualized in the context of the entire enzyme. This allowed us to examine both the importance of the NTD and the effect of the pathological mutations that map within this domain on the structure and function of GlnRS. The NTD of the yeast GlnRS was shown to be important for tRNA binding (33). In contrast, we show that the removal of both the N1 and N2 subdomains abolished the aminoacylation activity of hGlnRS, and that the deletion of the N1 subdomain decreased the k_{cat}/K_m by 270-fold (Table 2). This particular deletion affected the k_{cat} quite dramatically (≈130-fold decrease), while leaving the K_m almost unscathed (≈2-fold decrease). Likewise, the two pathological mutations that map within the NTD (i.e. G45V and Y57H) decrease the enzymatic activity of hGlnRS by affecting only the k_{cat} (Table 2). We therefore conclude that the NTD mutants are unable to form a productive complex with tRNA^{Gln}. Further, our results argue that the orientation of the NTD relative to the CATD is important for catalysis. Indeed, our kinetic data reveal that the H175A mutant, in which a single H-bond between the NTD and CATD domains is removed, exhibits a 60-fold lower k_{cat} and no change in K_m (Table 2). Besides effects on the catalysis, G45V and Y57H alter melting curves of GlnRS (Figure 4A), implying that these mutations affect both the fold and stability of the enzyme. It is, therefore, reasonable to speculate that the G45V and Y57H mutants cannot undergo a full conformational change upon tRNA binding and therefore cannot properly orient the 3′-end of the tRNA^{Gln} for catalysis. The crystal structures of the human GlnRS-tRNA^{Gln} complexes may explain this intriguing long-range communication between the NTD and the catalytic site.

Pathogenic mutations that map in CATD of human GlnRS cause protein misfolding and aggregation

Compound heterozygous mutations in human GlnRS were reported in multiple nonconsanguineous families to cause brain atrophy and disorders of the central nervous system (28,52,53). Of the four pathological mutations analyzed in this study, R403W and R515W inflict particularly harmful effects onto GlnRS. Our results show that both R403W and R515W can be overexpressed in *E. coli*, but that they are less soluble than the WT GlnRS, and that their soluble fraction is composed of misfolded protein associated with the bacterial chaperonin GroEL, mutant enzyme aggregates, and

partially degraded enzyme (Figures 4–6). In our studies, we used a combination of methods that included inspection of the purified material by electron microscopy, which provides an understanding of the identity of components present in the mixture and biochemical studies, which provide the functional context. Taken together, our findings are in agreement with the observation that the overexpression of R403W and R515W in neuronal cells results in protein aggregation and cellular toxicity (28). Hence, it is quite plausible that R403W and R515W contribute to the deterioration of neurons and the development of neurological disorders through enzyme misfolding, formation of aggregates, and partial degradation of the mutant GlnRS. Misfolded enzyme most likely would be targeted for degradation by proteasome and/or could be associated with chaperonins. However, it is also plausible that a low level of GlnRS activity may limit expression of the protein quality control machinery, making the misfolded GlnRS mutant proteins even more toxic. An individual carrying one of the Arg->Trp mutations would not display any phenotype because the WT enzyme that is encoded by the second allele would provide a sufficient level of enzymatic activity to sustain normal development. However, when combined with an allele carrying one of the reported NTD mutations, the GlnRS activity presumably plummets below tolerable levels and the phenotype arises. The GlnRS mutations may also perturb the overall chemical balance between L-glutamate and Gln, which could contribute to pathologies. Lastly, the phenotype caused by mutations in *QARS* is remarkably similar to the ones elicited by mutations in human *RARS2* (21), human *TSEN2*, *TSEN15*, *TSEN34,* and *TSEN54* (54), or by a knockdown of an important RNA splicing protein, *TSEN54*, in zebrafish (55). This would imply that GlnRS, ArgRS2, and TSEN complex are equally important during the same stages of development.

In conclusion, protein misfolding and aggregation are a hallmark of many neurodegenerative diseases such as Amyotrophic Lateral Sclerosis, and Parkinson's, Huntington's and Alzheimer's disease (56,57). To our knowledge, this is the first study to demonstrate that mutants of a human cytosolic aaRS, which are implicated in the disease of the central nervous system, are prone to misfolding and perhaps form aggregates. We suggest that these features of aaRSs be taken into account when neurological disorders are studied.

New developments

While completing this study, two reports describing additional pathological mutations in human *QARS* have been published. In one, Kodera *et al.* reported that compound heterozygous mutations, Y57H and K496*, cause early-onset epileptic encephalopathy (52), while in the other, Salvarinova *et al.* reported that R463* and Q742H mutations, which are encoded on separate alleles, elicit isolated supratentorial brain abnormalities (53). The latter phenotype is similar to the one described by Zhang *et al.* (28), but without visible abnormalities in the cerebellum. The association of the Y57H mutation in *QARS* with the disease has already been reported (8) and its effect on GlnRS structure and function is described herein. Given that R463* and K496* map in the CATD, it is likely that a non-functional protein is expressed, if any. The mRNAs of these mutants are probably targeted for the nonsense mediated mRNA decay, while the truncated nascent chains are good candidates for degradation on the proteasome. On the other hand, Q742H maps to the ABD, but it is not clear to what extent this particular mutation may affect the GlnRS activity. Further studies are thus needed to fully understand how pathological mutations affect *QARS* activity and the downstream cellular processes.

ACCESSION NUMBERS

The coordinates and structure factors are deposited in PDB with the accession codes 4YE6 (for WT hGlnRS), 4YE9 (for G45V) and 4YE8 (for Y57H).

SUPPLEMENTARY DATA

Supplementary Data are available at NAR Online.

ACKNOWLEDGEMENTS

We thank Zbyszek Otwinowski for help during phase calculation, Ruslan Sanishvili for help during data collection, Christopher Manzella for assistance during model building and refinement, Xiaochang Zhang and Christopher A. Walsh for help, discussions and suggestions.

FUNDING

Advanced Photon Source was supported by the U.S. DOE [DE-AC02-06CH11357]. The LS-CAT Sector 21 was supported by the Michigan Economic Development Corporation and the Michigan Technology Tri-Corridor [085P1000817]. The GM/CA@APS sector has been funded from the NCI [ACB-12002] and NIGMS [AGM-12006]. Kinetic analyses were supported by the National Institute of General Medical Sciences (NIGMS) of the National Institutes of Health (NIH) [R01 GM115431 to J.L.] and a startup fund from The University of Texas, Health Science Center at Houston [to J.L.]. The structure determination was supported by the grant from NIGMS [to M.S.]. Funding for open access charge: NIH.
Conflict of interest statement. None declared.

REFERENCES

1. Ibba,M. and Söll,D. (2000) Aminoacyl-tRNA synthesis. *Annu. Rev. Biochem.*, **69**, 617–650.
2. Schmidt,E. and Schimmel,P. (1994) Mutational isolation of a sieve for editing in a transfer RNA synthetase. *Science*, **264**, 265–267.
3. Mascarenhas,A.P., An,S., Rosen,A.E., Martinis,S.A. and Musier-Forsyth,K. (2008) In: RajBhandary,UL and Köhrer,C (eds). *Protein Engineering*. Springer-Verlag, NY, pp. 153–200.
4. Lo,W.S., Gardiner,E., Xu,Z., Lau,C.F., Wang,F., Zhou,J.J., Mendlein,J.D., Nangle,L.A., Chiang,K.P., Yang,X.L. *et al.* (2014) Human tRNA synthetase catalytic nulls with diverse functions. *Science*, **345**, 328–332.
5. Guo,M., Yang,X.L. and Schimmel,P. (2010) New functions of aminoacyl-tRNA synthetases beyond translation. *Nat. Rev. Mol. Cell. Biol.*, **11**, 668–674.
6. Xu,X., Shi,Y., Zhang,H.M., Swindell,E.C., Marshall,A.G., Guo,M., Kishi,S. and Yang,X.L. (2012) Unique domain appended to vertebrate tRNA synthetase is essential for vascular development. *Nat. Commun.*, **3**, 681.

7. Yao,P. and Fox,P.L. (2013) Aminoacyl-tRNA synthetases in medicine and disease. *EMBO Mol. Med.*, **5**, 332–343.
8. Antonellis,A. and Green,E.D. (2008) The role of aminoacyl-tRNA synthetases in genetic diseases. *Annu. Rev. Genomics Hum. Genet.*, **9**, 87–107.
9. Antonellis,A., Ellsworth,R.E., Sambuughin,N., Puls,I., Abel,A., Lee-Lin,S.Q., Jordanova,A., Kremensky,I., Christodoulou,K., Middleton,L.T. *et al.* (2003) Glycyl tRNA synthetase mutations in Charcot-Marie-Tooth disease type 2D and distal spinal muscular atrophy type V. *Am. J. Hum. Genet.*, **72**, 1293–1299.
10. Jordanova,A., Irobi,J., Thomas,F.P., Van Dijck,P., Meerschaert,K., Dewil,M., Dierick,I., Jacobs,A., De Vriendt,E., Guergueltcheva,V. *et al.* (2006) Disrupted function and axonal distribution of mutant tyrosyl-tRNA synthetase in dominant intermediate Charcot-Marie-Tooth neuropathy. *Nat. Genet.*, **38**, 197–202.
11. Latour,P., Thauvin-Robinet,C., Baudelet-Mery,C., Soichot,P., Cusin,V., Faivre,L., Locatelli,M.C., Mayencon,M., Sarcey,A., Broussolle,E. *et al.* (2010) A major determinant for binding and aminoacylation of tRNA(Ala) in cytoplasmic Alanyl-tRNA synthetase is mutated in dominant axonal Charcot-Marie-Tooth disease. *Am. J. Hum. Genet.*, **86**, 77–82.
12. McLaughlin,H.M., Sakaguchi,R., Liu,C., Igarashi,T., Pehlivan,D., Chu,K., Iyer,R., Cruz,P., Cherukuri,P.F., Hansen,N.F. *et al.* (2010) Compound heterozygosity for loss-of-function lysyl-tRNA synthetase mutations in a patient with peripheral neuropathy. *Am. J. Hum. Genet.*, **87**, 560–566.
13. Puffenberger,E.G., Jinks,R.N., Sougnez,C., Cibulskis,K., Willert,R.A., Achilly,N.P., Cassidy,R.P., Fiorentini,C.J., Heiken,K.F., Lawrence,J.J. *et al.* (2012) Genetic mapping and exome sequencing identify variants associated with five novel diseases. *PLoS One*, **7**, e28936.
14. Riley,L.G., Cooper,S., Hickey,P., Rudinger-Thirion,J., McKenzie,M., Compton,A., Lim,S.C., Thorburn,D., Ryan,M.T., Giege,R. *et al.* (2010) Mutation of the mitochondrial tyrosyl-tRNA synthetase gene, YARS2, causes myopathy, lactic acidosis, and sideroblastic anemia–MLASA syndrome. *Am. J. Hum. Genet.*, **87**, 52–59.
15. Bayat,V., Thiffault,I., Jaiswal,M., Tetreault,M., Donti,T., Sasarman,F., Bernard,G., Demers-Lamarche,J., Dicaire,M.J., Mathieu,J. *et al.* (2012) Mutations in the mitochondrial methionyl-tRNA synthetase cause a neurodegenerative phenotype in flies and a recessive ataxia (ARSAL) in humans. *PLoS Biol.*, **10**, e1001288.
16. Scheper,G.C., van der Klok,T., van Andel,R.J., van Berkel,C.G., Sissler,M., Smet,J., Muravina,T.I., Serkov,S.V., Uziel,G., Bugiani,M. *et al.* (2007) Mitochondrial aspartyl-tRNA synthetase deficiency causes leukoencephalopathy with brain stem and spinal cord involvement and lactate elevation. *Nat. Genet.*, **39**, 534–539.
17. Steenweg,M.E., Ghezzi,D., Haack,T., Abbink,T.E., Martinelli,D., van Berkel,C.G., Bley,A., Diogo,L., Grillo,E., Te Water Naude,J. *et al.* (2012) Leukoencephalopathy with thalamus and brainstem involvement and high lactate 'LTBL' caused by EARS2 mutations. *Brain*, **135**, 1387–1394.
18. Pierce,S.B., Chisholm,K.M., Lynch,E.D., Lee,M.K., Walsh,T., Opitz,J.M., Li,W., Klevit,R.E. and King,M.C. (2011) Mutations in mitochondrial histidyl tRNA synthetase HARS2 cause ovarian dysgenesis and sensorineural hearing loss of Perrault syndrome. *Proc. Natl. Acad. Sci. U.S.A.*, **108**, 6543–6548.
19. Pierce,S.B., Gersak,K., Michaelson-Cohen,R., Walsh,T., Lee,M.K., Malach,D., Klevit,R.E., King,M.C. and Levy-Lahad,E. (2013) Mutations in LARS2, encoding mitochondrial leucyl-tRNA synthetase, lead to premature ovarian failure and hearing loss in Perrault syndrome. *Am. J. Hum. Genet.*, **92**, 614–620.
20. Edvardson,S., Shaag,A., Kolesnikova,O., Gomori,J.M., Tarassov,I., Einbinder,T., Saada,A. and Elpeleg,O. (2007) Deleterious mutation in the mitochondrial arginyl-transfer RNA synthetase gene is associated with pontocerebellar hypoplasia. *Am. J. Hum. Genet.*, **81**, 857–862.
21. Glamuzina,E., Brown,R., Hogarth,K., Saunders,D., Russell-Eggitt,I., Pitt,M., de Sousa,C., Rahman,S., Brown,G. and Grunewald,S. (2012) Further delineation of pontocerebellar hypoplasia type 6 due to mutations in the gene encoding mitochondrial arginyl-tRNA synthetase, RARS2. *J. Inherit. Metab. Dis.*, **35**, 459–467.
22. Elo,J.M., Yadavalli,S.S., Euro,L., Isohanni,P., Gotz,A., Carroll,C.J., Valanne,L., Alkuraya,F.S., Uusimaa,J., Paetau,A. *et al.* (2012) Mitochondrial phenylalanyl-tRNA synthetase mutations underlie fatal infantile Alpers encephalopathy. *Hum. Mol. Genet.*, **21**, 4521–4529.
23. Taft,R.J., Vanderver,A., Leventer,R.J., Damiani,S.A., Simons,C., Grimmond,S.M., Miller,D., Schmidt,J., Lockhart,P.J., Pope,K. *et al.* (2013) Mutations in *DARS* cause hypomyelination with brain stem and spinal cord involvement and leg spasticity. *Am. J. Hum. Genet.*, **92**, 774–780.
24. Novarino,G., Fenstermaker,A.G., Zaki,M.S., Hofree,M., Silhavy,J.L., Heiberg,A.D., Abdellateef,M., Rosti,B., Scott,E., Mansour,L. *et al.* (2014) Exome sequencing links corticospinal motor neuron disease to common neurodegenerative disorders. *Science*, **343**, 506–511.
25. McMillan,H.J., Humphreys,P., Smith,A., Schwartzentruber,J., Chakraborty,P., Bulman,D.E., Beaulieu,C.L., Consortium,F.C., Majewski,J., Boycott,K.M. *et al.* (2015) Congenital visual impairment and progressive microcephaly due to lysyl-transfer ribonucleic acid (RNA) synthetase (KARS) mutations: the expanding phenotype of aminoacyl-transfer RNA synthetase mutations in human disease. *J. Child Neurol*, **30**, 1037–1043.
26. Guo,M. and Schimmel,P. (2013) Essential nontranslational functions of tRNA synthetases. *Nat. Chem. Biol.*, **9**, 145–153.
27. Abbott,J.A., Francklyn,C.S. and Robey-Bond,S.M. (2014) Transfer RNA and human disease. *Front. Genet.*, **5**, 158.
28. Zhang,X., Ling,J., Barcia,G., Jing,L., Wu,J., Barry,B.J., Mochida,G.H., Hill,R.S., Weimer,J.M., Stein,Q. *et al.* (2014) Mutations in QARS, encoding glutaminyl-tRNA synthetase, cause progressive microcephaly, cerebral-cerebellar atrophy, and Intractable seizures. *Am. J. Hum. Genet.*, **94**, 547–558.
29. Rould,M.A., Perona,J.J., Söll,D. and Steitz,T.A. (1989) Structure of E. coli glutaminyl-tRNA synthetase complexed with tRNA(Gln) and ATP at 2.8 A resolution. *Science*, **246**, 1135–1142.
30. Rho,S.B., Kim,M.J., Lee,J.S., Seol,W., Motegi,H., Kim,S. and Shiba,K. (1999) Genetic dissection of protein-protein interactions in multi-tRNA synthetase complex. *Proc. Natl. Acad. Sci. U.S.A.*, **96**, 4488–4493.
31. Kim,T., Park,S.G., Kim,J.E., Seol,W., Ko,Y.G. and Kim,S. (2000) Catalytic peptide of human glutaminyl-tRNA synthetase is essential for its assembly to the aminoacyl-tRNA synthetase complex. *J. Biol. Chem.*, **275**, 21768–21772.
32. Ko,Y.G., Kim,E.Y., Kim,T., Park,H., Park,H.S., Choi,E.J. and Kim,S. (2001) Glutamine-dependent antiapoptotic interaction of human glutaminyl-tRNA synthetase with apoptosis signal-regulating kinase 1. *J. Biol. Chem.*, **276**, 6030–6036.
33. Grant,T.D., Snell,E.H., Luft,J.R., Quartley,E., Corretore,S., Wolfley,J.R., Snell,M.E., Hadd,A., Perona,J.J., Phizicky,E.M. *et al.* (2012) Structural conservation of an ancient tRNA sensor in eukaryotic glutaminyl-tRNA synthetase. *Nucleic Acids Res.*, **40**, 3723–3731.
34. Grant,T.D., Luft,J.R., Wolfley,J.R., Snell,M.E., Tsuruta,H., Corretore,S., Quartley,E., Phizicky,E.M., Grayhack,E.J. and Snell,E.H. (2013) The structure of yeast glutaminyl-tRNA synthetase and modeling of its interaction with tRNA. *J. Mol. Biol.*, **425**, 2480–2493.
35. Otwinowski,Z. and Minor,W. (1997) In: Carter,CW Jr and Sweet,RM (eds). *Macromolecular Crystallography, part A*. Academic Press, NY, Vol. **276**, pp. 307–326.
36. Sheldrick,G.M. (2008) A short history of SHELX. *Acta Crystallogr. A*, **64**, 112–122.
37. Winn,M.D., Ballard,C.C., Cowtan,K.D., Dodson,E.J., Emsley,P., Evans,P.R., Keegan,R.M., Krissinel,E.B., Leslie,A.G., McCoy,A. *et al.* (2011) Overview of the CCP4 suite and current developments. *Acta Crystallogr. D Biol. Crystallogr.*, **67**, 235–242.
38. Wang,B.C. (1985) Resolution of phase ambiguity in macromolecular crystallography. *Methods Enzymol.*, **115**, 90–112.
39. Zhang,K.Y.J. and Main,P. (1990) Histogram matching as a new density modification technique for phase refinement and extension of protein molecules. *Acta Crystallogr. A*, **46**, 41–46.
40. Adams,P.D., Afonine,P.V., Bunkoczi,G., Chen,V.B., Davis,I.W., Echols,N., Headd,J.J., Hung,L.-W., Kapral,G.J., Grosse-Kunstleve,R.W. *et al.* (2010) PHENIX: a comprehensive Python-based system for macromolecular structure solution. *Acta Crystallogr. D*, **66**, 213–221.

41. Emsley,P. and Cowtan,K. (2004) Coot: model-building tools for molecular graphics. *Acta Crystallogr. D Biol. Crystallogr.*, **60**, 2126–2132.
42. Shindyalov,I.N. and Bourne,P.E. (1998) Protein structure alignment by incremental combinatorial extension (CE) of the optimal path. *Protein Eng.*, **11**, 739–747.
43. Schrödinger,LLC. (2010) http://www.schrodinger.com/.
44. Ito,T. and Yokoyama,S. (2010) Two enzymes bound to one transfer RNA assume alternative conformations for consecutive reactions. *Nature*, **467**, 612–616.
45. Brown,J.R. and Doolittle,W.F. (1999) Gene descent, duplication, and horizontal transfer in the evolution of glutamyl- and glutaminyl-tRNA synthetases. *J. Mol. Evol.* **49**, 485–495.
46. Kachroo,A.H., Laurent,J.M., Yellman,C.M., Meyer,A.G., Wilke,C.O. and Marcotte,E.M. (2015) Evolution. Systematic humanization of yeast genes reveals conserved functions and genetic modularity. *Science*, **348**, 921–925.
47. Lamour,V., Quevillon,S., Diriong,S., N'Guyen,V.C., Lipinski,M. and Mirande,M. (1994) Evolution of the Glx-tRNA synthetase family: the glutaminyl enzyme as a case of horizontal gene transfer. *Proc. Natl. Acad. Sci. U.S.A.*, **91**, 8670–8674.
48. Woese,C.R., Olsen,G.J., Ibba,M. and Söll,D. (2000) Aminoacyl-tRNA synthetases, the genetic code, and the evolutionary process. *Microbiol. Mol. Biol. Rev.*, **64**, 202–236.
49. Nureki,O., O'Donoghue,P., Watanabe,N., Ohmori,A., Oshikane,H., Araiso,Y., Sheppard,K., Söll,D. and Ishitani,R. (2010) Structure of an archaeal non-discriminating glutamyl-tRNA synthetase: a missing link in the evolution of Gln-tRNAGln formation. *Nucleic Acids Res.*, **38**, 7286–7297.
50. Sheppard,K., Yuan,J., Hohn,M.J., Jester,B., Devine,K.M. and Söll,D. (2008) From one amino acid to another: tRNA-dependent amino acid biosynthesis. *Nucleic Acids Res.*, **36**, 1813–1825.
51. O'Donoghue,P., Sheppard,K., Nureki,O. and Söll,D. (2011) Rational design of an evolutionary precursor of glutaminyl-tRNA synthetase. *Proc. Natl. Acad. Sci. U.S.A.*, **108**, 20485–20490.
52. Kodera,H., Osaka,H., Iai,M., Aida,N., Yamashita,A., Tsurusaki,Y., Nakashima,M., Miyake,N., Saitsu,H. and Matsumoto,N. (2015) Mutations in the glutaminyl-tRNA synthetase gene cause early-onset epileptic encephalopathy. *J. Hum. Genet.*, **60**, 97–101.
53. Salvarinova,R., Ye,C.X., Rossi,A., Biancheri,R., Roland,E.H., Pavlidis,P., Ross,C.J., Tarailo-Graovac,M., Wasserman,W.W. and van Karnebeek,C.D. (2015) Expansion of the QARS deficiency phenotype with report of a family with isolated supratentorial brain abnormalities. *Neurogenetics*, **16**, 145–149.
54. Budde,B.S., Namavar,Y., Barth,P.G., Poll-The,B.T., Nurnberg,G., Becker,C., van Ruissen,F., Weterman,M.A., Fluiter,K., te Beek,E.T. *et al.* (2008) tRNA splicing endonuclease mutations cause pontocerebellar hypoplasia. *Nat. Genet.*, **40**, 1113–1118.
55. Kasher,P.R., Namavar,Y., van Tijn,P., Fluiter,K., Sizarov,A., Kamermans,M., Grierson,A.J., Zivkovic,D. and Baas,F. (2011) Impairment of the tRNA-splicing endonuclease subunit 54 (tsen54) gene causes neurological abnormalities and larval death in zebrafish models of pontocerebellar hypoplasia. *Hum. Mol. Genet.*, **20**, 1574–1584.
56. Tyedmers,J., Mogk,A. and Bukau,B. (2010) Cellular strategies for controlling protein aggregation. *Nat. Rev. Mol. Cell. Biol.*, **11**, 777–788.
57. Hartl,F.U. and Hayer-Hartl,M. (2009) Converging concepts of protein folding *in vitro* and *in vivo*. *Nat. Struct. Mol. Biol.*, **16**, 574–581.